Earth and Planetary Science Letters 439 (2016) 182–193

Contents lists available at ScienceDirect

Earth and Planetary Science Letters

www.elsevier.com/locate/epsl

Northern Borneo stalagmite records reveal West Pacific hydroclimate across MIS 5 and 6

Stacy A. Carolin [a,*], Kim M. Cobb [a], Jean Lynch-Stieglitz [a], Jessica W. Moerman [a], Judson W. Partin [b], Syria Lejau [c], Jenny Malang [c], Brian Clark [c], Andrew A. Tuen [d], Jess F. Adkins [e]

[a] School of Earth and Atmospheric Sciences, Georgia Institute of Technology, Atlanta, GA, 30332, USA
[b] Institute for Geophysics, Jackson School of Geosciences, University of Texas, Austin, TX, 78758, USA
[c] Gunung Mulu National Park, Sarawak, Malaysia
[d] Institute of Biodiversity and Environmental Conservation, Universiti Malaysia Sarawak, 94300 Kota Samarahan, Malaysia
[e] Division of Geological and Planetary Sciences, California Institute of Technology, Pasadena, CA, 91125, USA

ARTICLE INFO

Article history:
Received 16 August 2015
Received in revised form 16 January 2016
Accepted 23 January 2016
Available online 11 February 2016
Editor: H. Stoll

Keywords:
speleothem
stable isotopes
glacial cycles
Termination 2
penultimate interglacial
tropical west Pacific

ABSTRACT

Over the past decades, tropical stalagmite $\delta^{18}O$ records have provided valuable insight on glacial and interglacial hydrological variability and its relationship to a variety of natural climate forcings. The transition out of the penultimate glaciation (MIS 6) represents an important target for tropical hydroclimate reconstructions, yet relatively few such reconstructions resolve this transition. Particularly, comparisons between Termination 1 and 2 provide critical insight on the extent and influence of proposed climate mechanisms determined from paleorecords and model experiments spanning the recent deglaciation. Here we present a new compilation of western tropical Pacific hydrology spanning 0–160 ky BP, constructed from eleven different U/Th-dated stalagmite $\delta^{18}O$ records from Gunung Mulu National Park in northern Borneo. The reconstruction exhibits significant precessional power in phase with boreal fall insolation strength over the 0–160 ky BP period, identifying precessional insolation forcing as the dominant driver of hydroclimate variability in northern Borneo on orbital timescales. A comparison with a network of paleoclimate records from the circum-Pacific suggests the insolation sensitivity may arise from changes in the Walker circulation system. Distinct millennial-scale increases in stalagmite $\delta^{18}O$, indicative of reduced regional convection, occur within glacial terminations and may reflect a response to shifts in inter-hemispheric temperature gradients. Our results imply that hydroclimate in this region is sensitive to external forcing, with a response dominated by large-scale temperature gradients.

1. Introduction

The hydrologic response to anthropogenic CO_2 forcing in the Indo-Pacific Warm Pool, a densely populated region, remains highly uncertain. Ambiguity persists due to a combination of high natural variability in hydroclimate, the limitations of short instrumental records of precipitation, and climate model biases in the simulation of present-day rainfall distributions (e.g. IPCC AR5, 2013). Hydroclimate reconstructions spanning the middle and late Pleistocene provide an opportunity to test the influence of several different climate forcings on tropical hydrology, with implications for hydroclimate sensitivity to past, present, and future greenhouse forcing.

Several long, tropical paleo-hydrology records from across the globe reveal the strong influence of precessional (23 ky) insolation on tropical monsoon strength, with some of the earliest evidence coming from the Indian Ocean (Prell and Kutzbach, 1987). More recently, stalagmite oxygen isotopic records with excellent absolute age control from the tropical–subtropical regions of Indo-China and South America (e.g. Cruz et al., 2005; Wang et al., 2008; Cheng et al., 2013) have demonstrated strong precessional (23 ky) signals closely in phase with local summer insolation. These signals are likely related to large-scale, coherent shifts in regional

* Corresponding author at: Department of Earth Sciences, University of Oxford, South Parks Road, Oxford, OX1 3AN, UK.
E-mail address: stacy.carolin@earth.ox.ac.uk (S.A. Carolin).

http://dx.doi.org/10.1016/j.epsl.2016.01.028
0012-821X/

monsoon systems, though the precise mechanisms underlying precessional rainfall $\delta^{18}O$ variability remain a subject of controversy (e.g. Clemens et al., 2010; Caley et al., 2014; Liu et al., 2014). In northern Borneo, stalagmite $\delta^{18}O$ records from Gunung Mulu National Park suggest that precession may be a dominant source of hydroclimate variability in the West Pacific Warm Pool (WPWP). During Marine Isotope Stage (MIS) 5a–c (70–100 ky BP) and the Holocene (0–10 ky BP), when precessional forcing is moderately strong, Mulu stalagmite $\delta^{18}O$ minima align with equatorial boreal fall insolation strength maxima (Carolin et al., 2013).

The extent of the influence of glacial boundary conditions relative to insolation forcing on western tropical Pacific convection is unclear. Trends in the 0–100 ky BP Mulu stalagmite $\delta^{18}O$ record showed little similarity with the trend in polar CO_2 and temperature records once mean ocean $\delta^{18}O$ variability due to ice volume changes had been removed from the stalagmite $\delta^{18}O$ values (Carolin et al., 2013). Further, little correspondence between Mulu stalagmite $\delta^{18}O$ and an index of Sunda Shelf areal extent was evident over the entire glacial cycle (Carolin et al., 2013). A Last Glacial Maximum (LGM) data-model inter-comparison, however, suggests the exposure of the Sunda shelf landmass as a first-order influence on large-scale tropical atmospheric circulation on glacial–interglacial timescales (DiNezio and Tierney, 2013). Termination 2 is an excellent target for additional inquiries regarding the relative contributions of glacial boundary conditions versus precessional insolation on equatorial western Pacific hydroclimate. While insolation forcing is relatively weak through the transition from the LGM into the deglaciation and through to the Holocene, large variations in insolation are coincident with the penultimate deglaciation.

On sub-orbital timescales, tropical–subtropical hydrological reconstructions and climate model studies confirm that abrupt climate change events have a profound impact on tropical–subtropical hydrological patterns, primarily through meridional migrations of the ITCZ and the major monsoon systems. Over the last deglaciation, for example, speleothem records from southeastern China, northern Borneo, Indonesia, and northern Australia provide a meridional transect of sites in the western Pacific that all show millennial-scale shifts in $\delta^{18}O$ coincident with North Atlantic cold intervals and in support of a southward migration of rainfall (Wang et al., 2001; Partin et al., 2007; Denniston et al., 2013a; Ayliffe et al., 2013). This pattern is repeated through MIS 3, where records exist (Wang et al., 2001; Carolin et al., 2013; Denniston et al., 2013b).

One important difference between Borneo stalagmite $\delta^{18}O$ and other southeast Asian stalagmite records is that the Borneo records reflect a relatively gradual trend into and out of maximum oxygen isotopic values (inferred as a dry period) associated with Heinrich Stadial 1 (HS1) (Partin et al., 2007). While the timing of the maximum dry event in northern Borneo is coincident with the other tropical–subtropical stalagmite records, the gradual trend in the Borneo record contrasts with other records' abrupt shifts into and out of their inferred weak (East Asian) or strong (Australian) HS1 monsoon intervals (Wang et al., 2001; Denniston et al., 2013a; Ayliffe et al., 2013). After H1, the Borneo stalagmites exhibit a relatively gradual deglaciation, with no clear Younger Dryas, suggesting that precession may dominate over remote forcing associated with the Bølling–Allerød and the Younger Dryas abrupt climate change events recorded in other tropical records (e.g. Partin et al., 2015). Pronounced $\delta^{18}O$ enrichments also characterize Borneo stalagmite $\delta^{18}O$ records preceding Terminations 3, 4, and 5, suggesting that H1-like enrichments are closely associated with deglaciations of the more distant past. However, these records, like many proxy records spanning these intervals, are associated with relatively large age uncertainties, preventing a robust analysis of phase relationships between climate forcings and northern Borneo convection during this time interval.

Here we present a high-resolution 70–160 ky BP multi-stalagmite $\delta^{18}O$ record from Gunung Mulu National Park, extending previously published Mulu $\delta^{18}O$ records across Termination 2. This study offers a detailed record of inferred northern Borneo rainfall variability over the Stage 5 warm periods and the penultimate deglaciation. We examine the power spectral density and phase alignment of the 0–160 ky records with 4°N insolation to determine the range of insolation forcing on northern Borneo rainfall through glacial/interglacial cycles. We then use the new Termination 2 Mulu $\delta^{18}O$ records to investigate the relative strength of insolation forcing versus glacial boundary conditions, comparing the northern Borneo hydrologic responses across Terminations 1 and 2.

2. Mulu Park's hydroclimate and karst

Gunung Mulu National Park's limestone outcrops are located on the north-western side of Borneo island (4°6′N, 114°53′E) (Fig. S1). The sample collection chambers are ~120–200 m above sea level (masl) with variable overlying limestone depths of ~50–150 m. Rainfall averages ~5000 mm annually, with no seasonality. As the ITCZ annually migrates north and south, Mulu's placement just north of the equator allows it to remain within West Pacific deep tropical convection year-round (Fig. 1). Large shifts in convective activity over Mulu occur inter-annually, during ENSO extremes. During an El Niño event, warm SSTs in the central and eastern Pacific drive convective activity eastward, leading to drier conditions over northern Borneo. During a La Niña event, convection strengthens over northern Borneo (Cobb et al., 2007).

A 5-yr daily rainfall collection study in Mulu shows present-day rainfall $\delta^{18}O$ variability to reflect regional precipitation amount with significant basin-wide correlations at monthly and longer timescales (Moerman et al., 2013), in agreement with isotope-enabled climate model simulations (Lewis et al., 2010). Long-term monthly Mulu rainfall $\delta^{18}O$ values demonstrate a weak semi-annual seasonal cycle (Moerman et al., 2013), despite a lack of seasonality in rainfall amount. The 5-yr rainwater isotope record shows two relative $\delta^{18}O$ minima in the winter and summer seasons, and two relative $\delta^{18}O$ maxima in the spring and fall seasons. As discussed in Moerman et al. (2013), the difference in isotopic values between the winter/summer months and the spring/fall months may be related to the wind dynamics in the region. During the boreal summer (winter), Mulu is on the outer limits of the ITCZ and winds have a strong southerly (northerly) trajectory (Fig. 1). The longer moisture trajectories associated with such winds may drive enhanced Raleigh fractionation leading to more depleted rainfall $\delta^{18}O$ during boreal summer and winter. Conversely, surface winds in northwestern Borneo are virtually non-existent during spring and fall seasons, with more local sources of moisture leading to relatively enriched rainfall $\delta^{18}O$ (Moerman et al., 2013). On intra-seasonal timescales, Moerman et al. (2013) shows multi-day rainfall anomalies in Mulu are closely associated with the wet phases of the Madden–Julian Oscillation (MJO). On inter-annual timescales, the Mulu rainfall $\delta^{18}O$ timeseries is significantly correlated to ENSO indices, which explain up to 40% of the monthly variance.

A 5-yr record of biweekly dripwater $\delta^{18}O$ values reflects the integration of amount-weighted rainfall $\delta^{18}O$ signals over the previous 3–10 months (Moerman et al., 2014), suggesting a short residence time of dripwater $\delta^{18}O$ relative to the multi-decadal to centennially resolved reconstructions of stalagmite $\delta^{18}O$ presented in this manuscript.

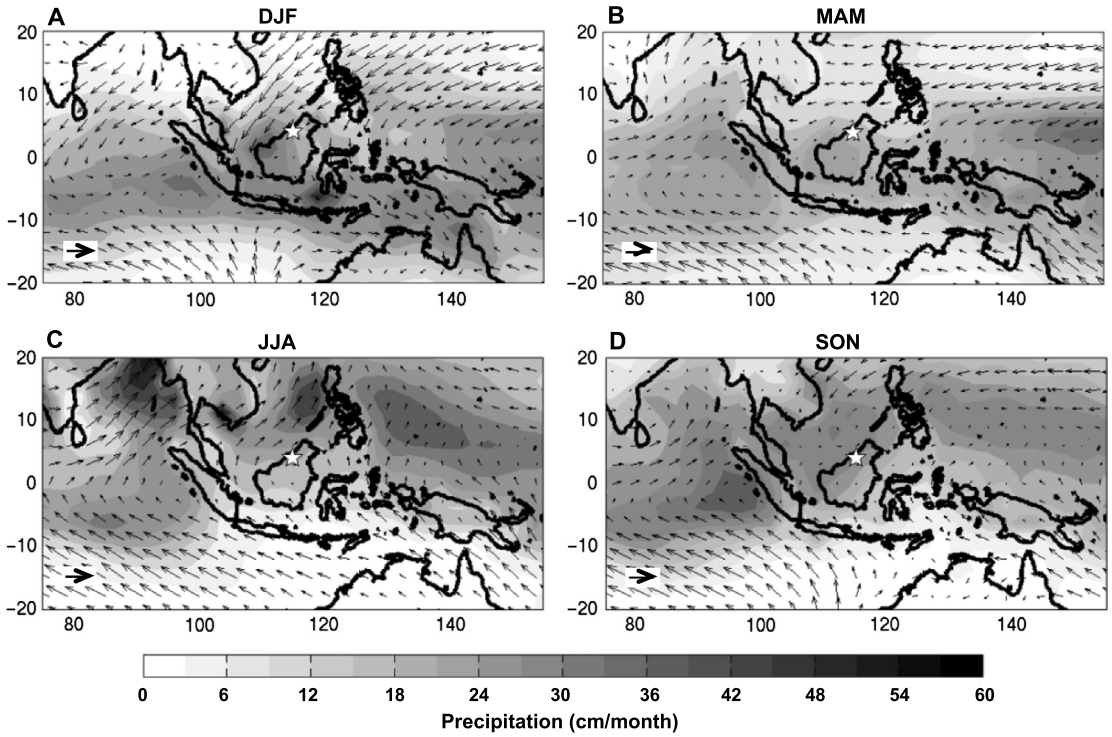

Fig. 1. Precipitation (shaded) and 1000 mb wind (arrows) climatology maps for the tropical Indo-Pacific, adopted from Cobb et al., 2007. (A) Mean precipitation and winds for December through February (DJF). A 5 m/s wind vector (shown in white box) is plotted for reference. (B) Same as (A) but for March through May (MAM). (C) Same as (A) but for June through August (JJA). (D) Same as (A) but for September through November (SON). CMAP precipitation (Xie and Arkin, 1997) and NCEP wind data (Kalnay et al., 1996) provided by the NOAA/OAR/ESRL PSD, Boulder, Colorado, USA, from their web-site at http://www.cdc.noaa.gov/.

3. Sample collection

Fallen stalagmites were collected during a 2012 expedition from (1) Fairy City chamber within Clearwater cave and (2) Whiterock cave (Fig. S1). After preliminary age analysis of the collected stalagmites, candidate samples were selected based on ^{238}U concentrations and extent of detrital contamination. New stalagmites analyzed in this study include FC12-12 (Fig. S2), FC12-14 (Fig. S3), and FC12-15 (Fig. S4) from Fairy City chamber and WR12-01 (Fig. S5) and WR12-12 (Fig. S6) from Whiterock Cave. Analyses were also continued from previous studies into the lower sections of SC03 (Fig. S7) and SC02 (Fig. S8), which were collected from Secret chamber within Clearwater cave during a 2006 expedition (Fig. S1).

4. Analytical methods

4.1. Stable oxygen isotope measurements

Oxygen isotopic analyses were conducted on 70–100 µg sample powders drilled at 0.2–1 mm increments, depending on individual stalagmite growth rates, along the central growth axis of the stalagmites. Drilling was completed using a RoundTool Laboratories 1.6 mm-diameter diamond-coated solid carbide end mill. Sampling procedure followed the continuous drilled "trough" technique along the growth axis to avoid aliasing. The δ^{18}O ratios were analyzed on either a Finnigan 253 or a Delta V Plus, both equipped with Kiel devices at the Georgia Institute of Technology (long-term reproducibility of less than $\pm 0.07‰$ (1σ), as determined by compiling >800 in-house aragonite standards run over the course of this study). Selected sections of the stalagmites were run twice on both instruments to confirm calibration and reproducibility. All δ^{18}O data are reported with respect to Vienna Peedee Belemnite (VPDB).

4.2. U-series isotope measurement and age calculation

Radiogenic U/Th analyses were conducted on 150–420 mg sample powders, with sample size chosen based on the ^{238}U concentration of the sample. Age samples were drilled along visual stalagmite lamina using a RoundTool Laboratories 0.8-mm or 1.6-mm diameter diamond-coated solid carbide end mill, with drill bit size chosen based on targeted sample volume. The U/Th dates were analyzed on a Finnigan Neptune MC-ICP-MS at the California Institute of Technology, following procedures outlined in Partin et al. (2007) and Carolin et al. (2013). The standard deviation (2σ) for the population of three or more procedural blank values within a batch was added in quadrature with the internal instrument standard error of the mean for all accepted isotope ratios (2σ). Measured concentrations and activity ratios are reported in Table S1 for all samples. Procedural blanks averaged ~0.1–5‰ of sample for both ^{230}Th and ^{234}U, with the spread due to the variation in U concentrations of the particular stalagmite samples.

The reported ages and their 2σ uncertainties (Table S1) were estimated using a Monte Carlo simulation that accounts for the errors in all isotope ratios and the uncertainty in the initial ^{230}Th/^{232}Th ratio (Section 4.3 and Supplementary Materials). If the relative age error was greater than 2% of the calculated age, the age was not used in constructing a stalagmite's age model. Also, if a repeat dating sample was drilled directly above or below a previously analyzed sample, the date with the smaller age error was used in constructing the age model.

4.3. Isochrons and ^{230}Th-corrected age model

Isochrons were used to correct for the detrital contributions of ^{238}U, ^{234}U, and ^{230}Th isotopes. Three or more co-precipitated samples with variable ^{232}Th/^{238}U ratios were analyzed on multiple stalagmites from multiple cave chambers for a total of 25

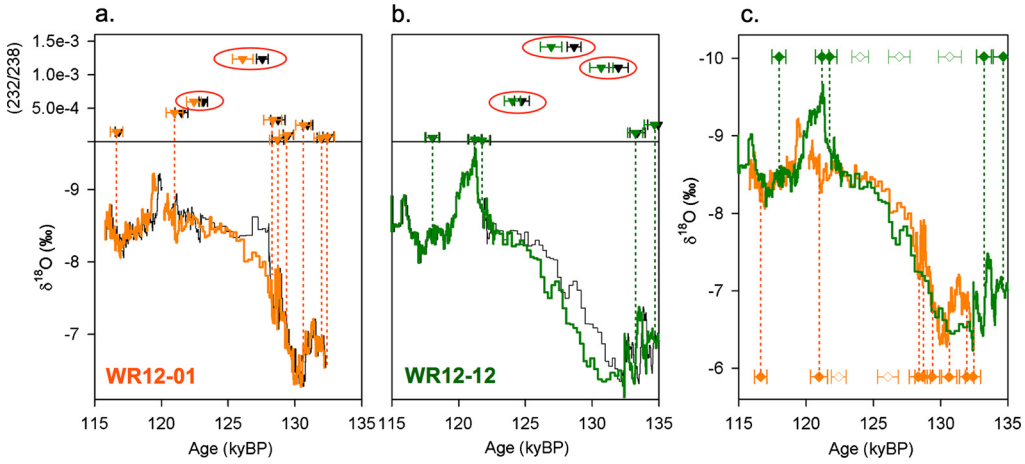

Fig. 2. Constraints on initial $^{230}Th/^{232}Th$ ratios for Whiterock stalagmite $\delta^{18}O$ timeseries. (a) WR12-01 age sample $^{232}Th/^{238}U$ versus age (values provided in Table S1) plotted above $\delta^{18}O$ versus age. Data calculated using initial $^{230}Th/^{232}Th$ atomic ratio = 60 ppm are plotted in orange, data calculated using initial $^{230}Th/^{232}Th$ atomic ratio = 4.4 ppm (bulk earth) are plotted in black. The $\delta^{18}O$ timeseries is plotted using the StalAge algorithm age model (Scholz and Hoffmann, 2011), which can change significantly due to a shift in age of the U/Th input data (see for example the 125–128 ky BP interval). Note a greater shift toward younger age occurs when U/Th age samples contain high ^{232}Th concentrations. Red circles highlight ages in which the 60 ppm Th-ratio age lies outside the error bars of the bulk-earth Th-ratio age. Vertical dotted lines indicate points on $\delta^{18}O$ timeseries corresponding to age samples with low ^{232}Th concentrations (<1000 ppt). (b) Same as (a) but for WR12-12. (c) WR12-01 and WR12-12 age samples with error bars (Supplementary Materials) and $\delta^{18}O$ timeseries. Age models were calculated using initial $^{230}Th/^{232}Th$ atomic ratio = 60 ± 20 ppm. Same vertical dotted lines as in (a) and (b). Ages of samples with ^{232}Th concentrations >1000 ppt are filled white.

isochron-derived initial $^{230}Th/^{232}Th$ ratios (Figs. S9–S10 and Table S2). A large scatter of $^{230}Th/^{232}Th$ values occurs in Mulu stalagmites as a whole, indicating that more than one source of initial ^{230}Th exists in our system. The detrital $^{230}Th/^{232}Th$ ratio for each stalagmite is therefore chosen based on multiple individual isochron values from either the same stalagmite, where available, or the same cave chamber. The detrital atomic $^{230}Th/^{232}Th$ ratios is assigned as follows, as determined in their original publications: SSC01 = 127 ± 20 ppm; SCH02 = 59 ± 13 ppm; BA04 = 55 ± 5 ppm; BA02 = 56 ± 11 ppm; SC03 and SC02 = 111 ± 41 ppm (2σ errors) (Partin et al., 2007; Carolin et al., 2013). Fairy City stalagmites are assigned a detrital atomic $^{230}Th/^{232}Th$ ratio = 78 ± 42 ppm (2σ errors) based on two isochrons (Supplementary Materials).

Due to relatively low levels of ^{232}Th in our Whiterock stalagmites, we were unable to calculate robust estimates of the initial $^{230}Th/^{232}Th$ ratio from isochrons (Fig. S10 and Table S2). In essence the drilled isochron samples were too 'clean' to give spread in the amount of ^{232}Th between different samples. To circumvent this problem, we compared overlapping $\delta^{18}O$ timeseries from our two Whiterock stalagmites using a spread of initial $^{230}Th/^{232}Th$ ratios. We used the $\delta^{18}O$ timeseries near ages of low detrital contamination in at least one stalagmite as targets, and assumed that both stalagmites' $\delta^{18}O$ records trend up toward depleted $\delta^{18}O$ values concurrently over the penultimate deglaciation. The initial atomic $^{230}Th/^{232}Th$ for Whiterock that produces the best fit between the two records is 60 ppm. We choose 20 ppm as the initial atomic $^{230}Th/^{232}Th$ 2σ error. Fig. 2 shows a comparison between the $\delta^{18}O$ timeseries using initial atomic $^{230}Th/^{232}Th$ ratios equal to 60 ppm (color) and bulk-earth 4.4 ppm (black) for both WR12-01 and WR12-12. Ages largely affected by initial ^{230}Th are highlighted. We note that the $\delta^{18}O$ maximum at 130 ky BP in WR12-01 is well constrained by several ages with low detrital Th contamination.

The age models for the stalagmites in this study were constructed using the StalAge algorithm (Scholz and Hoffmann, 2011) (Supplemental Materials). Age-depth profiles for FC12-12, FC12-14, FC12-15, WR12-01, WR12-12, and SC03 are provided in Figs. S2–S8 and S11. Secret and Whiterock stalagmites have the greatest U concentration (100–200 ppb and 200–500 ppb, respectively) and the least detrital contamination, and therefore are associated with the most robust age models (0.4–1.0% (2σ) relative age error, ±570 yrs (2σ) at Termination 2). FC12-14 and FC12-15 stalagmites have low U concentration (40–80 ppb) and larger detrital contamination, resulting in significantly larger age errors (0.7–4.2% (2σ) relative).

5. Results

This study presents five new Mulu $\delta^{18}O$ records to extend the previously published Mulu $\delta^{18}O$ records to 160 ky BP (Fig. 3). The stalagmite records are: WR12-01 (115.8–153.8 ky BP) and WR12-12 (113.9–144.4 ky BP) from Whiterock Cave, and FC12-12 (109.0–121.5 ky BP), FC12-14 (73.8–87.3 ky BP and 129.4–161.6 ky BP), and FC12-15 (139.9–164.0 ky BP) from Fairy City Chamber. We also extend previously published Secret Chamber stalagmites SC03 (103.5–119.5 ky BP addition) and SC02 (94.1–99.0 ky BP addition). Throughout most of the 0–160 ky BP record, two to four individual stalagmite records' growth periods overlap, confirming reproducibility of the Mulu $\delta^{18}O$ record at both orbital and millennial scales (Fig. 4). One gap in the record exists between 100–103 ky BP, as we were unable to identify a sample that covered that time interval.

The composite Mulu timeseries exhibits notable offsets in $\delta^{18}O$ between stalagmites, as observed in previous Mulu studies (e.g. Partin et al., 2007; Carolin et al., 2013). Drip water residence time and/or mixing in the vadose zone likely accounts for Mulu stalagmite offsets (Moerman et al., 2014). Partin et al. (2007) and Carolin et al. (2013) chose to reference all Gunung Buda/Mulu stalagmite $\delta^{18}O$ records to Snail Shell Cave stalagmite SCH02, originally published in Partin et al. (2007), for consistency. Following that protocol, the new stalagmite $\delta^{18}O$ records have been offset by the following amounts: WR12-01 and WR12-12 by +0.3‰, FC12-12 and FC12-14 by +0.35‰, and FC12-15, +0.6‰.

The 0–160 ky BP Mulu stalagmite $\delta^{18}O$ record exhibits significant orbital- and millennial-scale features. The maximum $\delta^{18}O$ enrichment at 130.6 ± 0.6 ky BP lasts ~500 yrs (age error determined by WR12-01, Fig. 2). This event is reproduced in two Whiterock cave stalagmites and one Fairy City chamber (Clearwater cave) stalagmite (Fig. 3), all positioned within a ~10 km radius (Fig. S1). The maximum $\delta^{18}O$ enrichment falls at the end of the 6000-yr "Weak Monsoon Interval" revealed in Chinese stalagmite records (e.g. Cheng et al., 2009), an interval which spans most of the global penultimate deglaciation. The average $\delta^{18}O$ values of

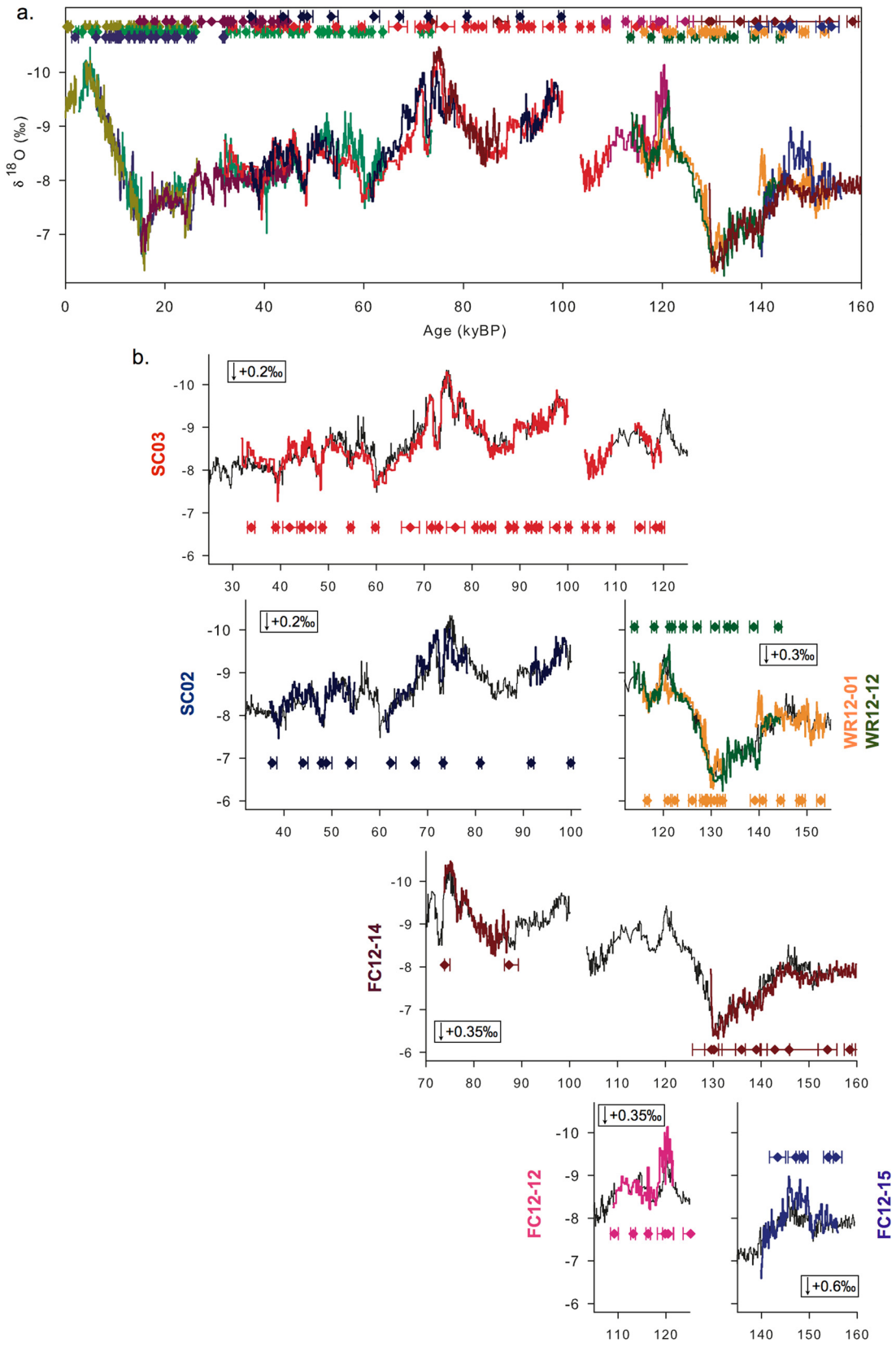

Fig. 3. Composite and individual Mulu stalagmite $\delta^{18}O$ records. (a) Overlapping Mulu stalagmite $\delta^{18}O$ records using StalAge age models (Scholz and Hoffmann, 2011): SC03 (red), SC02 (navy), FC12-14 (dark red), WR12-12 (dark green), WR12-01 (orange), FC12-12 (pink), and FC12-15 (purple), plotted with previously published stalagmite $\delta^{18}O$ data from our site (Partin et al., 2007; Carolin et al., 2013). (b) Individual Mulu stalagmite $\delta^{18}O$ records plotted on top of a Mulu stack (black) (100-yr non-overlapping boxcar averages). $\delta^{18}O$ offsets are shown in boxes on each individual plot. $\delta^{18}O$ offsets are chosen to match the absolute value of SCH02, consistent with the prior use of SCH02 as a benchmark (Partin et al., 2007). U/Th-based age samples plotted in corresponding colors, shown with 2σ uncertainty limits.

the last interglacial period (we define here as 115–125 ky BP) are ∼0.5‰ more enriched (drier) than the average last 500 yrs of the Mulu stalagmite $\delta^{18}O$ record, with three stalagmite records revealing an abrupt shift to depleted values (wet) from ∼121–119 ky BP, followed by a millennial-scale shift toward enriched values (dry) from ∼119–116 ky BP. Coming out of the last interglacial, the Mulu stalagmite $\delta^{18}O$ values demonstrate an overall trend toward more depleted (wetter) values from 120 to 75 ky BP, reaching the most depleted period of the 0–160 ky BP record (−1‰ difference from present day) near the beginning of the MIS 5a to 4 transition (∼75 ky BP).

In an effort to distinguish between the effects of ice-volume-related changes in stalagmite $\delta^{18}O$ versus hydroclimate-related changes in stalagmite $\delta^{18}O$ at our site, we create an "ice-volume corrected" $\delta^{18}O$ record, $\delta^{18}O_{IV\text{-}corr}$, by removing mean ocean $\delta^{18}O$ variability from the Mulu stalagmite $\delta^{18}O$ records. The mean ocean $\delta^{18}O_{SW}$ stack (Waelbroeck et al., 2002) aligns reasonably well with U–Th dated coral relative sea level (RSL) records for this time interval (see Fig. S14 for a detailed comparison between coral-derived sea level measurements and the mean ocean $\delta^{18}O_{SW}$ stack, a proxy for ice volume, over Termination 1 and Termination 2). As first recognized in Carolin et al. (2013), removing variability in mean ocean $\delta^{18}O_{SW}$ removes the Mulu $\delta^{18}O$ trend toward more enriched $\delta^{18}O$ values during MIS 3 evident on the original record. Removing the trend also shifts LGM values to values similar to the Mulu record's interglacial Stage 5e values (115–125 ky BP) (Fig. 4). Further, the maximum enrichment at Heinrich Stadial 1 (16.3 ky BP) is shifted approximately −1‰, while the large Mulu stalagmite $\delta^{18}O$ enrichment at 130.6 ky BP remains unaffected, due to the difference in relative timing between ice volume decay and the Mulu $\delta^{18}O$ millennial enrichment across the two terminations (Fig. 4).

Precessional-scale $\delta^{18}O$ variability, previously recognized in the younger Mulu stalagmite $\delta^{18}O$ records (Partin et al., 2007; Carolin et al., 2013), is evident throughout MIS 5 and 6 (70–160 ky BP). Spectral analysis confirms a significant peak at the precessional period in both the original and ice-volume corrected 0–160 ky BP records (Fig. 5a, see Supplementary Materials). The Mulu stalagmite $\delta^{18}O$ records slightly lag the precessional component of 4°N SON insolation (average September 1–November 31 insolation) (Fig. 5b, see Supplementary Materials). It follows that Mulu stalagmite $\delta^{18}O$ can also be described as out of phase with MAM precessional insolation, or in phase/out of phase with the insolation difference, SON-MAM or MAM-SON, as illustrated in Partin et al., 2007 (Fig. S12). The coherence between both the original and ice-volume corrected Mulu stalagmite $\delta^{18}O$ records and 4°N SON insolation at the precessional period is 0.93 and 0.94, respectively (Supplementary Materials).

6. Discussion

6.1. Insolation control on northern Borneo convection

Precessional forcing dominates the Mulu stalagmite $\delta^{18}O$ records, in line with other tropical stalagmite $\delta^{18}O$ records (e.g. Cruz et al., 2005; Wang et al., 2008; Cheng et al., 2013). The longest of these comes from China, where stalagmite $\delta^{18}O$ records spanning the last 224 ky show a large, significant precessional signal at ∼23 ky (e.g. Wang et al., 2008). However the difference in phasing between the Chinese monsoon records and the northern Borneo tropical Pacific records is significant: Chinese stalagmite $\delta^{18}O$ records slightly lag 4°N JJA insolation (average June 1–August 31 insolation), while Mulu stalagmite $\delta^{18}O$ records slightly lag 4°N SON insolation (average September 1–November 30 insolation) (Fig. 5b).

The boreal fall precessional sensitivity of Mulu stalagmite $\delta^{18}O$ may reflect changes in the properties of ENSO, given that ENSO

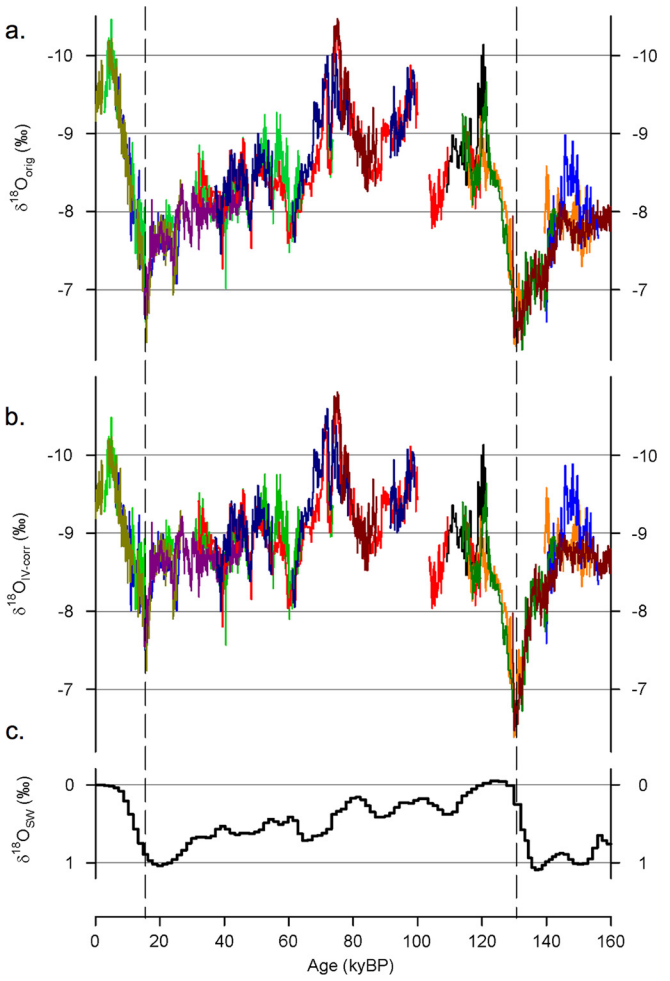

Fig. 4. Original and ice-volume corrected 0–160 ky BP Mulu stalagmite $\delta^{18}O$ records. (a) Original and (b) ice-volume corrected Mulu stalagmite $\delta^{18}O$ records (Partin et al., 2007; Carolin et al., 2013; this study). Ice-volume corrected Mulu records calculated by removing mean-ocean $\delta^{18}O_{SW}$ (Waelbroeck et al., 2002). (c) Mean ocean $\delta^{18}O_{SW}$ record constructed from temperature-corrected Atlantic–Pacific–Indian ocean sediment benthic-$\delta^{18}O$ stack (Waelbroeck et al., 2002). (c) was subtracted from (a) to construct (b).

variability explains the largest fraction of variance in the modern-day Mulu rainfall $\delta^{18}O$ timeseries (Moerman et al., 2013). Indeed, other orbital-scale tropical Pacific ENSO-dominated paleoclimate records support a precessional modulation of Walker circulation strength. A 1.2 My-long equatorial Pacific marine sediment nitrogen isotope ($\delta^{15}N$) gradient record, a proxy for upwelling rate and/or mean thermocline depth, has a strong signal at the precessional period (Rafter and Charles, 2012), as does an equatorial 240 ky-long marine record of the terrigenous fraction, a measure of local riverine runoff and precipitation, which was drilled from an eastern Indonesian site with weak seasonality (Dang et al., 2015).

Early investigations with the Cane–Zebiak model of intermediate complexity suggested that ENSO variance may be sensitive to boreal fall insolation owing to zonally asymmetric heating of the tropical Pacific in the late boreal summer/early fall (Clement et al., 1999). In boreal fall, the ITCZ moves north off of the equator in the east Pacific and divergent winds return to the eastern equatorial Pacific (EEP). Uniform surface ocean heating from solar forcing therefore results in larger heating of the atmosphere in the western equatorial Pacific (WEP) than the EEP. This asymmetric heating drives easterly winds and strengthens the Walker circulation. Clement et al. (1999) used this mechanism of zon-

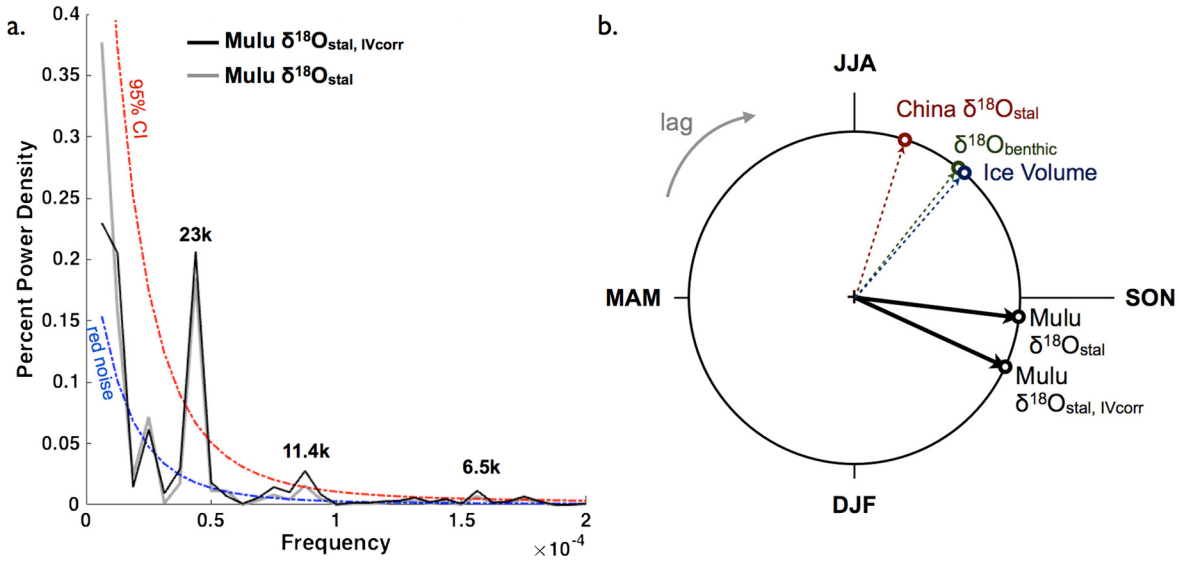

Fig. 5. Mulu stalagmite spectral analysis and phase wheel summary. (a) Percent power density from spectral analysis of original (grey) and ice-volume corrected (black) Mulu $\delta^{18}O$ composite stalagmite 0–160 ky BP record (100 yr sampling resolution) (Partin et al., 2007; Carolin et al., 2013; this study). (b) 23-ky period phase wheel diagram showing the phase alignment between the original and ice volume Mulu stalagmite 0–160 ky BP $\delta^{18}O$ record (black arrows) and 4°N latitude insolation (Berger, 1978). JJA indicates average insolation from June 1–August 31. Errors for Mulu across the 160 ky interval are approximately ±300 yrs, which translates into phase errors of ±5°. The phase relationship with the benthic foraminifera $\delta^{18}O$ stack (Lisiecki and Raymo, 2005), derived sea level (Waelbroeck et al., 2002), and the Chinese stalagmite $\delta^{18}O$ records (Wang et al., 2001, 2008) is also indicated in the phase wheel diagram. Errors for Chinese stalagmite $\delta^{18}O$ across the 160 ky interval are similar to the Mulu stalagmite errors. Errors for the marine records are approximately ±4000 yrs, which translates into phase errors of ±18°. DPSS taper method spectral analysis and multi-taper method coherence were done using a Matlab script provided by Prof. Peter Huybers (www.people.fas.harvard.edu/~phuybers/Mfiles/Toolbox/) (details provided in Supplementary Materials).

ally asymmetric atmospheric heating to relate Milankovitch forcing to tropical climate. The Zebiak–Cane ENSO model shows that a disruption of this seasonal cycle impacts ENSO frequency, due to nonlinear interactions that exist between the seasonal cycle and inter-annual variability (e.g. Zebiak and Cane, 1987; Tziperman et al., 1997). Clement et al. (1999) ran the Zebiak–Cane ENSO model over 150 ky at 10-day time-steps to show that Milankovitch forcing can produce a similar model response. The authors concluded that nonlinear interactions between the system's response to Milankovitch forcing on seasonal and inter-annual timescales yields a change in ENSO frequency, which they define as a mean tropical climate change due to the change in the statistics of events (Clement et al., 1999). A warm, El Niño (cold, La Niña) mean state occurred when the Zebiak–Cane ENSO model was forced by anomalous cooling (warming) in the late summer/early fall (Clement et al., 1999).

The high sensitivity of modern-day Mulu rainfall $\delta^{18}O$ to ENSO variability (Moerman et al., 2013) makes changes in the strength of the Walker circulation a plausible explanation for the observed precessional signal in Mulu stalagmite $\delta^{18}O$ that slightly lags SON insolation at the same latitude. High ENSO variance periods are likely to be manifested in a multi-decadal resolution Mulu stalagmite $\delta^{18}O$ record as enriched $\delta^{18}O$ periods because El Niño events produce higher amplitude Mulu rainfall $\delta^{18}O$ anomalies than La Niña events (Moerman et al., 2013, 2014). Precessional-scale Mulu stalagmite $\delta^{18}O$ maxima are indeed aligned with SON insolation minima throughout the 0–160 ky BP record (Fig. 6), in agreement with the hypothesis that coupled minimum fall insolation and maximum spring insolation leads to a decrease in the zonal SST gradient, priming the tropical Pacific for warm, El Niño events. Further, a recent synthesis of paleo-ENSO reconstructions spanning much of the Holocene uncovers significant reductions in central Pacific ENSO variance during the 3–5 ky BP interval (Emile-Geay et al., 2015), a period when boreal fall insolation is at a maximum. However, available ENSO-resolving datasets are still too sparse to address whether the 3–5 ky BP minimum in ENSO properties was driven by precessional forcing or internal variability in the climate system. Nevertheless, both the LR04-tuned (Lisiecki and Raymo, 2005) equatorial Pacific nitrogen isotope record (Rafter and Charles, 2012), a proxy for upwelling rate and/or mean thermocline depth, and the Mulu stalagmite $\delta^{18}O$ record, a proxy for regional precipitation in an ENSO-affected area, are aligned with SON insolation (Fig. 6). This agreement raises the possibility that the observed changes in Holocene ENSO properties uncovered in high-resolution proxy data reflect a sensitivity to boreal fall precessional forcing.

Although the dominant peak in the Mulu stalagmite $\delta^{18}O$ spectral analysis is at the precessional period, a smaller, yet significant, 11.5 ky peak (Fig. 5a) suggests seasonal forcing as a possible driver of Mulu stalagmite $\delta^{18}O$ variability. This is consistent with the fact that the sun passes overhead twice per year – once during spring and once during fall – which would imply a sensitivity to both spring and fall precessional forcing. Indeed, modern Mulu rainwater $\delta^{18}O$ does exhibit a weak semi-annual cycle, with relative maxima in both boreal spring and fall (Moerman et al., 2013). Moerman et al. (2013) hypothesized that weak regional winds during the spring and fall seasons may result in shorter water vapor trajectories and less cumulative isotopic fractionation during these seasons. Further investigations into the mechanisms underlying the observed seasonal cycle in modern rainfall $\delta^{18}O$, ideally employing an isotope-enabled atmospheric GCM, would help to clarify the role of seasonal rainfall $\delta^{18}O$ variations in contributing to fall precessional sensitivity in Mulu stalagmite $\delta^{18}O$.

6.2. $\delta^{18}O$ enrichments on glacial terminations

Termination 1 and Termination 2 are both characterized by large $\delta^{18}O$ maxima in Mulu stalagmite $\delta^{18}O$, implying relatively dry conditions in the equatorial West Pacific during these times. Such events are reminiscent of the weak monsoon intervals identified in the stalagmite $\delta^{18}O$ records from China (e.g. Cheng et al., 2009). However, Mulu $\delta^{18}O$ trends gradually into and out of the isotope maxima, unlike the more abrupt changes seen for the Chinese stalagmites. In addition, the timing of Mulu $\delta^{18}O$ max-

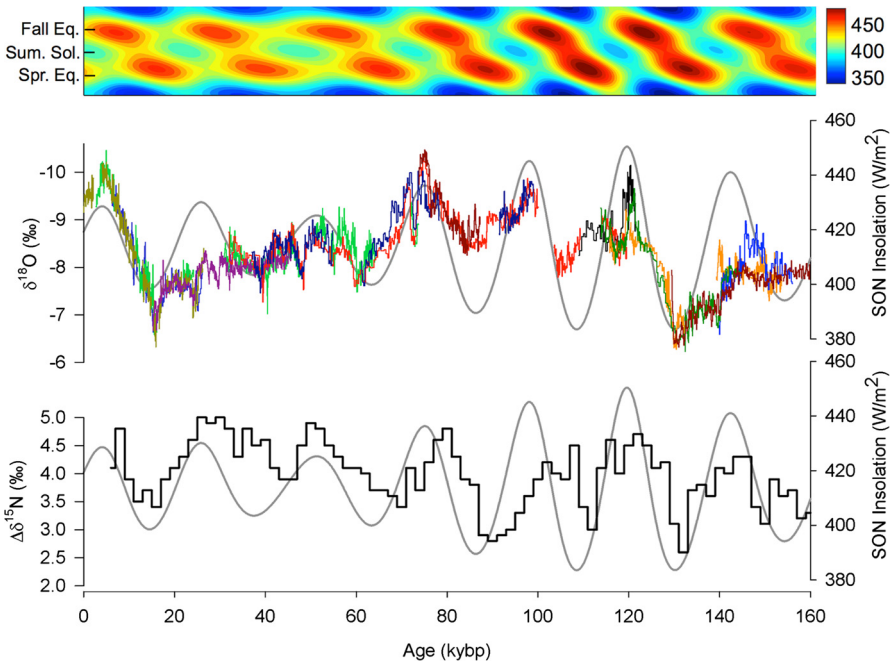

Fig. 6. Comparison of both Mulu stalagmite $\delta^{18}O$ records and equatorial Pacific marine sediment $\Delta\delta^{15}N$ records with 4°N SON insolation (average Sept. 1–Nov. 30 insolation strength). (Top) Contour plot of latitude 4°N insolation flux (W/m^2) daily through the calendar year from 0–160 ky BP. (Middle) Mulu stalagmite $\delta^{18}O$ records (Partin et al., 2007; Carolin et al., 2013; this study) with overlapping 4°N SON insolation. (Lower) Equatorial Pacific marine sediment $\Delta\delta^{15}N$ records tuned to LR04 age model (Rafter and Charles, 2012) with overlapping 4°N SON insolation.

ima with respect to atmospheric CO_2, high latitude temperatures, and ice volume differs between the two Terminations (Fig. 7). In Termination 1, Mulu reaches its $\delta^{18}O$ maximum when CO_2 and temperature have risen to only about 1/3 of their interglacial values, while in Termination 2, Mulu reaches its $\delta^{18}O$ maximum when CO_2 and temperature have risen to almost their full interglacial values (see Supplementary Materials for discussion of ice core age models) (Fig. 7). This behavior is in contrast to the Chinese stalagmites, which have been used to set the timing of terminations across a wide range of high latitude data (Cheng et al., 2009).

The Mulu $\delta^{18}O$ record tracks boreal fall insolation into and out of the Mulu $\delta^{18}O$ maximum throughout both Terminations, despite the Mulu $\delta^{18}O$ maxima's difference in timing with other glacial forcings (Fig. 7). This phasing implies that precessional insolation forcing might play a role in driving northern Borneo convection across major deglaciations. However, a direct relationship between northern Borneo convection and boreal fall insolation is not supported by the composite Mulu $\delta^{18}O$ record (Partin et al., 2007; Meckler et al., 2012; Carolin et al., 2013; this study), which spans five glacial Terminations (Fig. 8). The amplitudes of the Mulu $\delta^{18}O$ maxima during Terminations do not correlate to the size of fall insolation peaks – Termination 5 (defined here as ~431 ky BP) is one of the largest $\delta^{18}O$ enrichments but insolation forcing is small (Fig. 8). As such, while fall insolation is correlated with the timing of Mulu $\delta^{18}O$ maxima, other factors likely determine the relative size of the anomaly.

The magnitude of enrichments in Mulu stalagmite $\delta^{18}O$ across glacial Terminations may be related to movement of the annual position of the ITCZ. Several previous studies have invoked southward ITCZ migrations to explain tropical drying associated with Heinrich events during the last deglaciation and throughout MIS 3 (e.g. Peterson et al., 2000; Wang et al., 2001; Partin et al., 2007; Cheng et al., 2013; Carolin et al., 2013; Ayliffe et al., 2013). A possible link between Mulu drying and inter-hemispheric climate changes comes from modeling studies implying a dynamical link between changes in cross-equatorial heat transport, driven by inter-hemispheric temperature gradients, and meridional shifts in the ITCZ (Kang et al., 2008; Donohoe et al., 2013). In general the ITCZ moves towards the warmer hemisphere, and the large differences in polar temperatures across deglaciations may have driven large meridional shifts in the ITCZ. Indeed, a correlation has been observed between the magnitude of Antarctic warmings and the duration of North Atlantic stadials in the polar ice cores (EPICA Members, 2006). It is possible that during the early phases of deglaciations, the fact that warming in Antarctica preceded warming in the high-latitude Northern Hemisphere may explain large shifts in the position of the ITCZ that are reflected in the pronounced Borneo stalagmite $\delta^{18}O$ enrichments.

A related issue raised by our new record is the degree to which 100-ky power is evident in tropical precipitation. While there is no hint of the classic 'sawtooth' structure in the Chinese stalagmites, there is some indication of 100-ky cyclicity in the extended Mulu $\delta^{18}O$ data, as well as tropical Pacific SST (Fig. 8). We argue that any 100-ky cycle visible in the Mulu stalagmite $\delta^{18}O$ records is principally due to two factors: the deglacial $\delta^{18}O$ enrichments and the global ocean $\delta^{18}O$ variance with glaciation. Subtracting the mean ocean ice-volume effect from the Mulu $\delta^{18}O$ record shows a nearly flat glacial to interglacial trend over the last 160 ky (Fig. 4). Notably, the minimum $\delta^{18}O$ over the last cycle is at MIS 5a, not 5e, where there is peak SST warming and highest pCO_2. Indeed, spectral analysis of the 0–570 ky BP Mulu $\delta^{18}O$ record corrected for changes in mean ocean $\delta^{18}O$ due to ice volume shows only a slightly significant signal at the 100-ky period, forced by the large and consistent $\delta^{18}O$ enrichments at Terminations (Fig. S13, Supplementary Materials). The weak effect of global boundary conditions on northern Borneo rainfall contrasts markedly with the strong correlation found between greenhouse gas forcing and tropical Pacific SSTs (e.g. Lea, 2004; Herbert et al., 2010). However, model simulations also indicate that tropical hydrologic variability may vary independently of global ice volume changes, and is instead largely governed by changes in large-scale temperature gradients (Clement et al., 2004). Alternatively, SST responds more directly to changes in heat fluxes as-

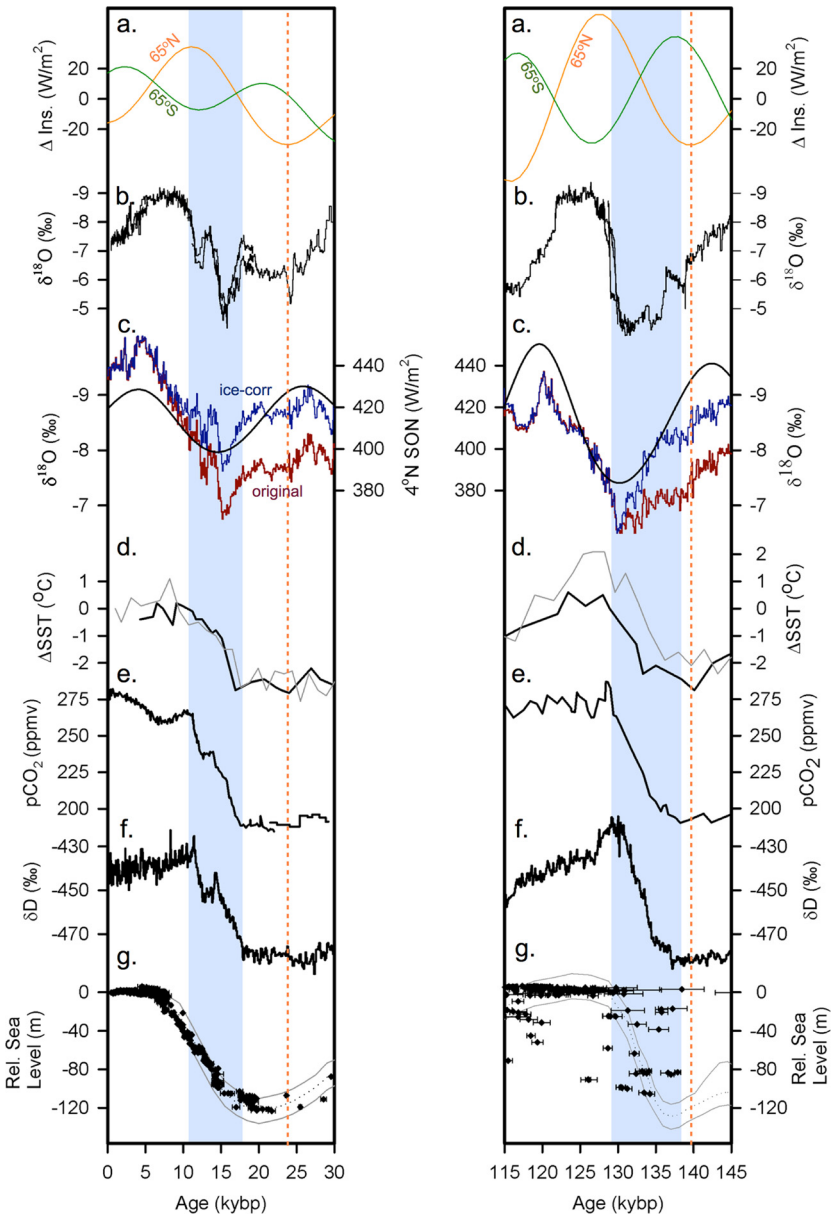

Fig. 7. (Left) Termination 1 paleorecord comparison. (a) Insolation forcing (W/m^2) at 65°N boreal summer solstice (orange) and 65°S austral summer solstice (green) (Berger, 1978). (b) Chinese δ^{18}O stalagmite records (Wang et al., 2001, 2008). (c) Composite Mulu stalagmite δ^{18}O records, original published (dark red) and ice-volume corrected (blue) (Partin et al., 2007; Carolin et al., 2013) averaged in 100 yr boxcar bins with overlapping 4°N SON insolation (average Sept. 1–Nov. 30 insolation strength) (Berger, 1978). (d) Marine sediment Mg/Ca SST reconstructions from WEP site ODP 806b (black) (Lea et al., 2000) and EEP site TR163-22 (grey) (Lea et al., 2006) on published age model. SST_{0K} set as 29 °C for site ODP 806b and 24.3 °C for TR163-22, per the present day SST listed in original publications. (e) EDC CO_2 records (Monnin et al., 2001) on the EDC3 timescale and Taylor Dome CO_2 records (Indermühle et al., 1999) on the st9810 timescale (see Supplementary Materials for age model details). (f) Vostok ice core δD records (Petit et al., 1999) on the Lemieux–Dudon timescale (see Supplementary Materials for age model details). (g) Coral relative sea level records (Supplementary Materials, see Fig. S14) plotted on top of minimum and maximum (grey) and mean (grey dotted) ocean temperature-corrected δ^{18}O records (Waelbroeck et al., 2002). (Right) Termination 2 paleorecord comparison. (a) Same as left. (b) Sanbao stalagmite δ^{18}O records (Wang et al., 2008; Cheng et al., 2009). (c) Composite Mulu stalagmite δ^{18}O records, original (red) and ice-volume corrected (blue) (this study) averaged in 100 yr boxcar bins with overlapping 4°N SON insolation (Berger, 1978). (d) Same as left. (e) Vostok ice core CO_2 record (Petit et al., 1999). Age model determined by aligning Vostok ice core CH_4 record with Sanbao δ^{18}O record (see Supplementary Materials for details). (f) Vostok ice core δD records (Petit et al., 1999). Age model determined by aligning Vostok ice core CH_4 record with Sanbao δ^{18}O record (see Supplementary Materials for details). (g) Same as left. Blue shading indicates the interval of deglaciation CO_2 rise. The orange vertical dashed line marks the 65°N NH summer insolation minimum prior to the Termination. (For interpretation of the references to color in this figure legend, the reader is referred to the web version of this article.)

sociated with glacial–interglacial variability. Other multi-hundred–thousand-year tropical hydrologic records also demonstrate significant signals at the precessional period with little power at the 100-ky period (e.g. Tachikawa et al., 2011; Thomas et al., 2014; Dang et al., 2015).

Models and proxy records suggest that exposure of the Sunda and Sahel Shelves drove changes in convection over Borneo (e.g. DiNezio and Tierney, 2013), raising the prospect that inundation of the Sunda Shelf during glacial terminations may have contributed to the observed Mulu deglaciation δ^{18}O enrichments. Indeed, there is probably a large change in the relative albedo and heat capacity of the Maritime Continent with glacial sea level change as this region has a large concentration of shallow seas. Additionally, exposure of the Sunda Shelf likely would have had an effect to some extent on the seasonal cycle of rainwater isotopes in Mulu. However, a comparison between the Termination 1 and Termination 2 sea level records reveals significant differences regarding the timing of Sunda Shelf inundation and Mulu δ^{18}O enrichment. During Termi-

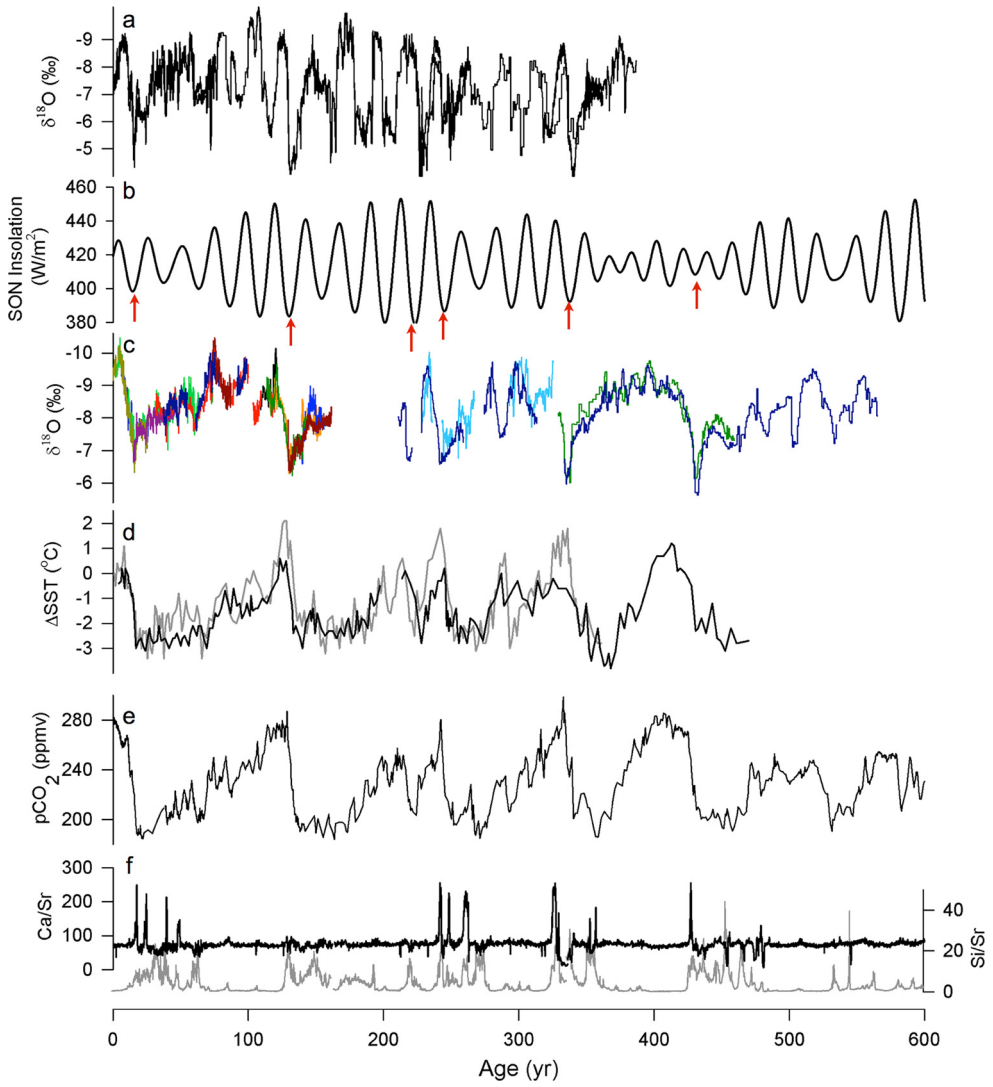

Fig. 8. Comparison of 0–600 ky BP global paleorecords. (a) Chinese stalagmite $\delta^{18}O$ records (Wang et al., 2001, 2008; Cheng et al., 2009). (b) Timeseries of SON insolation (average Sept. 1–Nov. 30 insolation strength) at latitude 4°N (Berger, 1978). Red arrows show timing of Mulu $\delta^{18}O$ maxima on terminations. (c) Mulu stalagmite $\delta^{18}O$ records (Partin et al., 2007; Meckler et al., 2012; Carolin et al., 2013; this study). Records are not ice-volume corrected. (d) Marine sediment Mg/Ca SST reconstructions from WEP site ODP 806b (black) and EEP site TR163-19 (grey) on published age models (Lea et al., 2000; Lea, 2004). (e) Vostok CO_2 records (Petit et al., 1999) on the EDC3 timescale (see Supplementary Materials for age model details). (f) Ca/Sr ratios (suggested indicator of Hudson Straight Heinrich layers) and Si/Sr ratios (suggested indicator of different sources and/or glaciological processes than Hudson Straight Heinrich layers) from XRF scan of IODP Site U1308 (reoccupation of DSDP 609) ocean sediment core (Hodell et al., 2008). (For interpretation of the references to color in this figure legend, the reader is referred to the web version of this article.)

nation 1, Mulu $\delta^{18}O$ trends into its large $\delta^{18}O$ enrichment while sea level remains below 100 m and the Sunda Shelf remains exposed (Hanebuth et al., 2000). Alternatively, during Termination 2, Mulu $\delta^{18}O$ trends into its large $\delta^{18}O$ enrichment while the Sunda Shelf is being completely inundated (Fig. S14; see Supplementary Materials). By 130 ky BP, the timing of the maximum Mulu $\delta^{18}O$ enrichment on Termination 2, many coral records agree that the sea-level high stand has already been reached and that the Sunda Shelf is already flooded (Fig. S14; see Supplementary Materials). Based on this evidence, the Mulu records suggest that neither exposure nor inundation of the Sunda Shelf on its own is causing large northern Borneo rainfall anomalies on glacial terminations, though we cannot rule out a role for large climate sensitivity in this region as sea level flooding alters the local atmosphere's surface boundary condition.

7. Conclusions

The extended Mulu stalagmite $\delta^{18}O$ record suggests that on orbital timescales, northern Borneo hydrology is relatively insensitive to glacial–interglacial variability, and is largely controlled by boreal fall precessional forcing. We hypothesize that the phase relationship between Mulu $\delta^{18}O$ and boreal fall insolation reflects changes in the strength of the Walker circulation, perhaps reflecting forced changes in ENSO properties – a mechanism supported by several other tropical Pacific records. The close alignment of Mulu $\delta^{18}O$ with boreal fall insolation is maintained through both Termination 1 and Termination 2, despite markedly different phasing of glacial boundary conditions across each termination. However, the amplitudes of large Mulu $\delta^{18}O$ maxima that occur during Terminations do not correlate with the size of fall insolation peaks, therefore factors other than 4°N boreal fall insolation strength likely determine the relative size of the large Mulu $\delta^{18}O$ Termination maxima. The large magnitude and timing of the Mulu $\delta^{18}O$ enrichments observed during glacial terminations present a compelling target for paleoclimate modeling studies aimed at resolving the mechanisms of glacial–interglacial variability.

Acknowledgements

We thank Danja Mewes, Eleanor Middlemas, and Sang Chen for fieldwork assistance, and all the staff at Gunung Mulu National Park World Heritage Site for their dedicated assistance during field expeditions. We also thank Guillaume Paris, Sophie Hines, James Rae, and Andrea Burke for their assistance in U–Th dating, and Hussein Sayani, Pamela Grothe, and Tammy Chang for their assistance in oxygen isotope measurements. The research was funded by NSF PECASE Award #0645291 and NSF AGS Award #1502830 to KMC, NSF AGS award #0903099 to JFA, and a NSF Graduate Research Fellowship to SAC. Permits for this work were granted by the Malaysian Economic Planning Unit, the Sarawak State Planning Unit, and the Sarawak Forestry Department. All data reported in this paper are archived at NCDC (ftp://ftp.ncdc.noaa.gov/pub/data/paleo/speleothem/pacific/gunung-mulu2016.txt).

Appendix A. Supplementary material

Supplementary material related to this article can be found online at http://dx.doi.org/10.1016/j.epsl.2016.01.028.

References

Ayliffe, L.K., Gagan, M.K., Zhao, J.X., Drysdale, R.N., Hellstrom, J.C., Hantoro, W.S., Griffiths, M.L., Scott-Gagan, H., St Pierre, E., Cowley, J.A., Suwargadi, B.W., 2013. Rapid interhemispheric climate links via the Australasian monsoon during the last deglaciation. Nat. Commun. 4.

Berger, A.L., 1978. Long-term variations of daily insolation and quaternary climatic changes. J. Atmos. Sci. 35, 2362–2367.

Caley, T., Roche, D.M., Renssen, H., 2014. Orbital Asian summer monsoon dynamics revealed using an isotope-enabled global climate model. Nat. Commun. 5.

Carolin, S.A., Cobb, K.M., Adkins, J.F., Clark, B., Conroy, J.L., Lejau, S., Malang, J., Tuen, A.A., 2013. Varied response of western Pacific hydrology to climate forcings over the Last Glacial Period. Science 340, 1564–1566.

Cheng, H., Edwards, R.L., Broecker, W.S., Denton, G.H., Kong, X.G., Wang, Y.J., Zhang, R., Wang, X.F., 2009. Ice age terminations. Science 326, 248–252.

Cheng, H., Sinha, A., Cruz, F.W., Wang, X.F., Edwards, R.L.A., d'Horta, F.M., Ribas, C.C., Vuille, M., Stott, L.D., Auler, A.S., 2013. Climate change patterns in Amazonia and biodiversity. Nat. Commun. 4.

Clemens, S.C., Prell, W.L., Sun, Y., 2010. Orbital-scale timing and mechanisms driving Late Pleistocene Indo-Asian summer monsoons: reinterpreting cave speleothem $\delta^{18}O$. Paleoceanography 25.

Clement, A.C., Seager, R., Cane, M.A., 1999. Orbital controls on the El Niño/Southern Oscillation and the tropical climate. Paleoceanography 14, 441–456.

Clement, A.C., Hall, A., Broccoli, A.J., 2004. The importance of precessional signals in the tropical climate. Clim. Dyn. 22, 327–341.

Cobb, K.M., Adkins, J.F., Partin, J.W., Clark, B., 2007. Regional-scale climate influences on temporal variations of rainwater and cave dripwater oxygen isotopes in northern Borneo. Earth Planet. Sci. Lett. 263, 207–220.

Cruz, F.W., Burns, S.J., Karmann, I., Sharp, W.D., Vuille, M., Cardoso, A.O., Ferrari, J.A., Dias, P.L.S., Viana, O., 2005. Insolation-driven changes in atmospheric circulation over the past 116,000 years in subtropical Brazil. Nature 434, 63–66.

Dang, H., Jian, Z., Kissel, C., Bassinot, F., 2015. Precessional changes in the western equatorial Pacific hydroclimate: a 240 kyr marine record from the Halmahera Sea, East Indonesia. Geochem. Geophys. Geosyst. 16, 148–164.

Denniston, R.F., Asmerom, Y., Lachniet, M., Polyak, V.J., Hope, P., An, N., Rodzinyak, K., Humphreys, W.F., 2013a. A Last Glacial Maximum through middle Holocene stalagmite record of coastal Western Australia climate. Quat. Sci. Rev. 77, 101–112.

Denniston, R.F., Wyrwoll, K.H., Asmerom, Y., Polyak, V.J., Humphreys, W.F., Cugley, J., Woods, D., LaPointe, Z., Peota, J., Greaves, E., 2013b. North Atlantic forcing of millennial-scale Indo-Australian monsoon dynamics during the Last Glacial period. Quat. Sci. Rev. 72, 159–168.

DiNezio, P.N., Tierney, J.E., 2013. The effect of sea level on glacial Indo-Pacific climate. Nat. Geosci. 6, 485–491.

Donohoe, A., Marshall, J., Ferreira, D., McGee, D., 2013. The relationship between ITCZ location and cross-equatorial atmospheric heat transport: from the seasonal cycle to the Last Glacial Maximum. J. Climate 26, 3597–3618.

Emile-Geay, J., Cobb, K.M., Carre, M., Braconnot, P., Leloup, J., Zhou, Y., Harrison, S.P., Correge, T., McGregor, H.V., Collins, M., Driscoll, R., Elliot, M., Schneider, B., Tudhope, A., 2015. Links between tropical Pacific seasonal, interannual and orbital variability during the Holocene. Nat. Geosci. http://dx.doi.org/10.1038/ngeo2608.

EPICA Members, 2006. One-to-one coupling of glacial climate variability in Greenland and Antarctica. Nature 444, 195–198.

Hanebuth, T., Stattegger, K., Grootes, P.M., 2000. Rapid flooding of the Sunda Shelf: a late-glacial sea-level record. Science 288, 1033–1035.

Herbert, T.D., Peterson, L.C., Lawrence, K.T., Liu, Z.H., 2010. Tropical ocean temperatures over the past 3.5 million years. Science 328, 1530–1534.

Hodell, D.A., Channell, J.E.T., Curtis, J.H., Romero, O.E., Rohl, U., 2008. Onset of "Hudson Strait" Heinrich events in the eastern North Atlantic at the end of the middle Pleistocene transition (similar to 640 ka)? Paleoceanography 23.

Indermühle, A., Stocker, T.F., Joos, F., Fischer, H., Smith, H.J., Wahlen, M., Deck, B., Mastroianni, D., Tschumi, J., Blunier, T., Meyer, R., Stauffer, B., 1999. Holocene carbon-cycle dynamics based on CO_2 trapped in ice at Taylor Dome, Antarctica. Nature 398, 121–126.

IPCC, 2013. Climate change 2013: the physical science basis. In: Stocker, T.F., et al. (Eds.), Contribution of Working Group I to the Fifth Assessment Report of the Intergovernmental Panel on Climate Change. Cambridge Univ. Press.

Kalnay, E., Kanamitsu, M., Kistler, R., Collins, W., Deaven, D., Gandin, L., Iredell, M., Saha, S., White, G., Woollen, J., Zhu, Y., Chelliah, M., Ebisuzaki, W., Higgins, W., Janowiak, J., Mo, K.C., Ropelewski, C., Wang, J., Leetmaa, A., Reynolds, R., Jenne, R., Joseph, D., 1996. The NCEP/NCAR 40-year reanalysis project. Bull. Am. Meteorol. Soc. 77, 437–471.

Kang, S.M., Held, I.M., Frierson, D.M.W., Zhao, M., 2008. The response of the ITCZ to extratropical thermal forcing: idealized slab-ocean experiments with a GCM. J. Climate 21, 3521–3532.

Lea, D.W., 2004. The 100,000-yr cycle in tropical SST, greenhouse forcing, and climate sensitivity. J. Climate 17, 2170–2179.

Lea, D.W., Pak, D.K., Spero, H.J., 2000. Climate impact of late quaternary equatorial Pacific sea surface temperature variations. Science 289, 1719–1724.

Lea, D.W., Pak, D.K., Belanger, C.L., Spero, H.J., Hall, M.A., Shackleton, N.J., 2006. Paleoclimate history of Galapagos surface waters over the last 135,000 yr. Quat. Sci. Rev. 25, 1152–1167.

Lewis, S.C., LeGrande, A.N., Kelley, M., Schmidt, G.A., 2010. Water vapour source impacts on oxygen isotope variability in tropical precipitation during Heinrich events. Clim. Past 6, 325–343.

Lisiecki, L.E., Raymo, M.E., 2005. A Pliocene–Pleistocene stack of 57 globally distributed benthic $\delta^{18}O$ records. Paleoceanography 20.

Liu, Z., Wen, X., Brady, E.C., Otto-Bliesner, B., Yu, G., Lu, H., Cheng, H., Wang, Y., Zheng, W., Ding, Y., Edwards, R.L., Cheng, J., Liu, W., Yang, H., 2014. Chinese cave records and the East Asia Summer Monsoon. Quat. Sci. Rev. 83, 115–128.

Meckler, A.N., Clarkson, M.O., Cobb, K.M., Sodemann, H., Adkins, J.F., 2012. Interglacial hydroclimate in the Tropical West Pacific through the Late Pleistocene. Science 336, 1301–1304.

Moerman, J.W., Cobb, K.M., Adkins, J.F., Sodemann, H., Clark, B., Tuen, A.A., 2013. Diurnal to interannual rainfall $\delta^{18}O$ variations in northern Borneo driven by regional hydrology. Earth Planet. Sci. Lett. 369, 108–119.

Moerman, J.W., Cobb, K.M., Partin, J.W., Meckler, A.N., Carolin, S.A., Adkins, J.F., Lejau, S., Malang, J., Clark, B., Tuen, A.A., 2014. Transformation of ENSO-related rainwater to dripwater $\delta^{18}O$ variability by vadose water mixing. Geophys. Res. Lett. 41, 7907–7915.

Monnin, E., Indermühle, A., Dällenbach, A., Flückiger, J., Stauffer, B., Stocker, T.F., Raynaud, D., Barnola, J.M., 2001. Atmospheric CO_2 concentrations over the last glacial termination. Science 291, 112–114.

Partin, J.W., Cobb, K.M., Adkins, J.F., Clark, B., Fernandez, D.P., 2007. Millennial-scale trends in west Pacific warm pool hydrology since the Last Glacial Maximum. Nature 449, 452–453.

Partin, J.W., Quinn, T.M., Shen, C.C., Okumura, Y., Cardenas, M.B., Siringan, F.P., Banner, J.L., Lin, K., Hu, H.M., Taylor, F.W., 2015. Gradual onset and recovery of the Younger Dryas abrupt climate event in the tropics. Nat. Commun. 6.

Peterson, L.C., Haug, G.H., Hughen, K.A., Rohl, U., 2000. Rapid changes in the hydrologic cycle of the tropical Atlantic during the last glacial. Science 290, 1947–1951.

Petit, J.R., Jouzel, J., Raynaud, D., Barkov, N.I., Barnola, J.M., Basile, I., Bender, M., Chappellaz, J., Davis, M., Delaygue, G., Delmotte, M., Kotlyakov, V.M., Legrand, M., Lipenkov, V.Y., Lorius, C., Pepin, L., Ritz, C., Saltzman, E., Stievenard, M., 1999. Climate and atmospheric history of the past 420,000 years from the Vostok ice core, Antarctica. Nature 399, 429–436.

Prell, W.L., Kutzbach, J.E., 1987. Monsoon variability over the past 150,000 years. J. Geophys. Res., Atmos. 92, 8411–8425.

Rafter, P.A., Charles, C.D., 2012. Pleistocene equatorial Pacific dynamics inferred from the zonal asymmetry in sedimentary nitrogen isotopes. Paleoceanography 27.

Scholz, D., Hoffmann, D.L., 2011. StalAge – an algorithm designed for construction of speleothem age models. Quat. Geochronol. 6, 369–382.

Tachikawa, K., Cartapanis, O., Vidal, L., Beaufort, L., Barlyaeva, T., Bard, E., 2011. The precession phase of hydrological variability in the Western Pacific Warm Pool during the past 400 ka. Quat. Sci. Rev. 30, 3716–3727.

Thomas, E.K., Clemens, S.C., Prell, W.L., Herbert, T.D., Huang, Y., Liu, Z., Damste, J.S.S., Sun, Y., Wen, X., 2014. Temperature and leaf wax δ^2H records demonstrate seasonal and regional controls on Asian monsoon proxies. Geology 42, 1075–1078.

Tziperman, E., Zebiak, S.E., Cane, M.A., 1997. Mechanisms of seasonal – ENSO interaction. J. Atmos. Sci. 54, 61–71.
Waelbroeck, C., Labeyrie, L., Michel, E., Duplessy, J.C., McManus, J.F., Lambeck, K., Balbon, E., Labracherie, M., 2002. Sea-level and deep water temperature changes derived from benthic foraminifera isotopic records. Quat. Sci. Rev. 21, 295–305.
Wang, Y.J., Cheng, H., Edwards, R.L., An, Z.S., Wu, J.Y., Shen, C.C., Dorale, J.A., 2001. A high-resolution absolute-dated Late Pleistocene monsoon record from Hulu Cave, China. Science 294, 2345–2348.
Wang, Y.J., Cheng, H., Edwards, R.L., Kong, X.G., Shao, X.H., Chen, S.T., Wu, J.Y., Jiang, X.Y., Wang, X.F., An, Z.S., 2008. Millennial- and orbital-scale changes in the East Asian monsoon over the past 224,000 years. Nature 451, 1090–1093.
Xie, P.P., Arkin, P.A., 1997. Global precipitation: a 17-year monthly analysis based on gauge observations, satellite estimates, and numerical model outputs. Bull. Am. Meteorol. Soc. 78, 2539–2558.
Zebiak, S.E., Cane, M.A., 1987. A model El Niño southern oscillation. Mon. Weather Rev. 115, 2262–2278.